



Juvenile magma recognition and eruptive dynamics inferred from the analysis of ash time series: The 2015 reawakening of Cotopaxi volcano



H. Elizabeth Gaunt^{a,*}, Benjamin Bernard^a, Silvana Hidalgo^a, Antonio Proaño^a, Heather Wright^b, Patricia Mothes^a, Evelyn Criollo^c, Ulrich Kueppers^d

^a Instituto Geofísico, Escuela Politécnica Nacional, Quito, Ecuador

^b U.S. Geological Survey and USAID Office of Foreign Disaster Assistance, Volcano Disaster Assistance Program (VDAP), Cascades Volcano Observatory, 1300 SE Cardinal Court, Vancouver, WA 98683, USA

^c Departamento de Metalurgia Extractiva, Escuela Politécnica Nacional, Quito, Ecuador

^d Ludwig-Maximilians-Universität München, Earth and Environmental Sciences, Munich, Germany

ARTICLE INFO

Article history:

Received 4 July 2016

Received in revised form 19 October 2016

Accepted 22 October 2016

Available online 26 October 2016

Keywords:

Volcanic ash

Volcano monitoring

Cotopaxi volcano

Eruption dynamics

Hazard assessment

ABSTRACT

Forecasting future activity and performing hazard assessments during the reactivation of volcanoes remain great challenges for the volcanological community. On August 14, 2015 Cotopaxi volcano erupted for the first time in 73 years after approximately four months of precursory activity, which included an increase in seismicity, gas emissions, and minor ground deformation. Here we discuss the use of near real-time petrological monitoring of ash samples as a complementary aid to geophysical monitoring, in order to infer eruption dynamics and evaluate possible future eruptive activity at Cotopaxi. Twenty ash samples were collected between August 14 and November 23, 2015 from a monitoring site on the west flank of the volcano. These samples contain a range of grain types that we classified as: hydrothermal/altered, lithic, juvenile, and free crystals. The relative proportions of these grains evolved as the eruption progressed, with increasing amounts of juvenile material and a decrease in hydrothermally altered material. In samples from the initial explosion, juvenile grains are glassy, microlite-poor and contain hydrothermal minerals (opal and alunite). The rising magma came in contact with the hydrothermal system under confinement, causing hydro-magmatic explosions that cleared the upper part of the plumbing system. Subsequently, the magmatic column produced a thermal aureole in the conduit and dried out the hydrothermal system, allowing for dry eruptions. Magma ascent rates were low enough to allow for efficient outgassing and microlite growth. Constant supply of magma from below caused quasi-continuous disruption of the uppermost magma volume through a combination of shear-deformation and gas expansion. The combination of increasing crystallinity of juvenile grains, and high measured SO₂ flux indicate decreasing integrated magma ascent rates and clearing of the hydrothermal system along transport pathways in a system open to gas loss. The near real-time monitoring of ash samples combined with traditional geophysical monitoring techniques during the reawakening of Cotopaxi allowed us to gain a much clearer understanding of events than when using traditional geophysical monitoring alone.

© 2016 Elsevier B.V. All rights reserved.

1. Introduction

The reactivation of andesitic volcanoes is commonly preceded by weeks to months of increased seismicity, deformation and/or increased SO₂ emissions (e.g., Sparks, 2003). This precursory activity can include small explosions and ash emissions (e.g., Cashman and Hoblitt, 2004). These explosions are commonly interpreted as phreatic or phreatomagmatic, where heat from the rising magma interacts with water in the sub-surface such as in a shallow hydrothermal system (Macdonald, 1972 and Sheridan and Wohletz, 1981). The monitoring

of geophysical, geodetic and geochemical signals from volcanoes has greatly improved our ability to forecast and interpret present and impending eruptive activity. Based on these data, empirical pattern recognition and deterministic and probabilistic models may be used to forecast eruptions (Sparks, 2003). These forecasts can be improved by the addition of petrologic monitoring to investigate the nature of material ejected during early, small volume explosive eruptions (e.g., Cashman and Hoblitt, 2004). By classifying ash grains into lithologic and textural categories, and tracking their variations through time, information can be learned about the nature of the explosions, their source depths, the timing of formation of pathways from the magma reservoir to the surface, and the rate at which magma ascends through that pathway (e.g., Ersoy et al., 2006; Miwa et al., 2013; Wright et al.,

* Corresponding author.

E-mail address: egaunt@igepn.edu.ec (H.E. Gaunt).

2012). Quantitative characterization of ash includes measurement of grain size, mineral composition, ash grain morphology, particle crystallinity and vesicularity, and componentry of constituents (e.g., Cioni et al., 2014; Eychenne et al., 2012).

The recognition of juvenile magma in ash can be difficult, especially where older rocks from the volcanic edifice are similar in composition through time, or where juvenile fragments are highly crystalline (see Pardo et al., 2014). Conventionally, juvenile ash is distinguished based on highly vesicular and/or glassy texture (Watanabe et al., 1999), absence of pervasive alteration, and compositional and mineralogical homogeneity (Cioni et al., 2008). However, studies of the ash from the precursory explosions of Mount St. Helens before the climactic eruption on the 18 May 1980 have shown that the textures of juvenile material are greatly affected by decompression and degassing-driven crystallization (Cashman and Hoblitt, 2004). Ash from Mount St. Helens was only recognized as juvenile after its texture was found to be similar to the cryptodome fragments ejected on 18 May 1980 and during subsequent eruptions. Since then, highly crystalline, microlite-rich ash fragments have been recognized as juvenile magma at many volcanoes around the world. For example, at Sakurajima volcano, the distinction between juvenile fragments is not based on crystallinity, but surface texture and luster (Miwa et al., 2009). Additionally, crystal textures can be widely variable within a single eruption (e.g., 1999–2006 Tungurahua eruptions, Wright et al., 2012). The crystal textures of volcanic materials are controlled by their history of decompression, degassing, and cooling. At relatively high degrees of undercooling (due to relatively rapid cooling, decompression and/or H₂O-loss), crystal nucleation dominates over growth and the resultant crystals are numerous and small in size (e.g., Hammer and Rutherford, 2002 and Shea and Hammer, 2013). Small crystals or microlites (<40 μm) therefore provide important information about magmatic processes just prior to or during eruption. For example, crystallinity was found to decrease with: 1) increasing magma supply rate and therefore eruption style at Etna, Tungurahua and Eyjafjallajökull volcanoes (Taddeucci et al., 2004; Wright et al., 2012 and Cioni et al., 2014), 2) decreasing repose interval (and thus possible shallow residence time) at Pinatubo volcano prior to its climactic eruption (Hammer et al., 1999), and 3) increasing lava effusion rate at Unzen volcano (Nakada and Motomura, 1999).

The August 2015 reawakening of Cotopaxi Volcano provides an exceptional opportunity to study the temporal evolution of ash through the initial stages of renewed eruptive activity. The first ash samples were collected immediately after the initial explosions and sampled frequently through the three and a half months of eruptive activity. We use standard analysis and characterization techniques to track changes in erupted material. Scanning electron microscope (SEM) analysis of both fresh and polished sections was combined with componentry analysis with a stereoscopic microscope to show the textural and compositional evolution of the ash. We use these observations to identify juvenile magma and inform discussion regarding the eruptive dynamics and the importance of continuously monitoring eruptive products as a complementary aid to classical geophysical monitoring and eruption forecasting.

2. Cotopaxi volcano

Cotopaxi volcano is a 5987 m high ice-capped stratovolcano located in the eastern cordillera of the Ecuadorian Andes (Fig. 1A). The volcano lies 50 km south of the capital city of Quito, Ecuador and has produced both andesitic and rhyolitic eruptive products over its ~560 kyr history (Hall and Mothes, 2008). Andesitic volcanism has dominated the eruptive history of Cotopaxi over the past 4400 years, producing andesitic lava flows, lapilli and ash falls, pyroclastic flows, and triggering lahars with runout distances of up to 325 km (e.g., Mothes and Vallance, 2015). Cotopaxi has erupted several times within the historic record, producing Plinian eruptions and long-lived phases of variably explosive eruptive activity (Pistolesi et al., 2011). Based on historic accounts,



Fig. 1. Location map of Cotopaxi volcano and photo taken on 03/09/2015 during an overflight mission by the Instituto Geofísico to measure thermal anomalies and perform multi-gas measurements.

several of these eruptive phases began with many months of precursory activity. However, unrest has not always led to eruption. In 2001–2002, a period of seismic and geodetic unrest occurred at Cotopaxi, including an inferred intrusion of $20 \times 10^6 \text{ m}^3$ of magma (Molina et al., 2008; Hickey et al., 2015).

Five eruptive cycles have been recorded during the historical period (since 1532) with paroxysms ranging between VEI 3 and 4 (Pistolesi et al., 2011). The most intense eruptions occurred in 1532–1534, 1742–1744, 1766–1768, 1853–1854 and 1877. With the exception of the 1853 event, each of the other eruptive periods resulted in VEI 4 events, which included regional ash and lapilli falls, pyroclastic flows, and especially the generation of large lahars. Typical tephra fallout volumes are 0.1 to 0.2 km³ (DRE) (Barberi et al., 1995; Hall and Mothes, 2008; Pistolesi et al., 2011). Based on historical records and stratigraphy, eruptive activity at Cotopaxi follows repose periods that ranged from 200 years to a mere 22 years. Past activity included some clusters of events, separated by longer periods of quiescence (Hall and Mothes, 2008 and Pistolesi et al., 2011). Eruptions commonly began with vent-clearing Vulcanian explosions producing abundant altered conduit-plugging rock. Subsequently, after the initial conduit opening, sub-Plinian to Plinian activity ensued, during which regional ash and lapilli

falls were produced, mostly directed to the W-NW of the cone and depositing a mm-thick dusting of ash in Quito (Hall and Mothes, 2008). Before Cotopaxi's June 1877 eruption, the detonation sounds produced by ascending gas breaking through the conduit plug were loud enough to have been heard in Pasto, Colombia and Guayaquil, Ecuador (both over 250 km away) (Hall and Mothes, 2008). These strong booms occurred a day before the onset of the main eruption (VEI 4) on 26 June 1877. Cotopaxi's historically erupted magmas generally comprise two pyroxene andesites with 57–62 wt% SiO₂, 1.2–1.7 wt% K₂O, and a phenocryst assemblage that includes plagioclase, hypersthene, augite, magnetite and olivine (Hall and Mothes, 2008).

2.1. The 2015 reawakening of Cotopaxi

The extensive monitoring of Cotopaxi volcano performed by the Instituto Geofísico (IG), of the Escuela Politécnica Nacional (Quito, Ecuador), documents temporal observational and geophysical changes in the volcanic system. The current period of volcanic unrest began in April 2015. An increase in the number of long-period (LP) seismic events per time and size (Fig. 2) at the beginning of April, coupled with small but definite changes in the deformation of the flanks of the volcano (≤ 1.5 cm, tiltmeter data) signaled the start of this new eruptive phase. In May, SO₂ flux from the summit crater began to increase as well, with values increasing from background lower than 100 tons/day up to 3000 tons/day (Hidalgo et al., 2016). This coincided with the period of maximum frequency of LP events (>160 LP on May 28 (IGEPN Special Report number 22, 6 November, 2015)) and was followed, on June 4, by the first appearance of seismic tremor. Small fumarolic and gas plumes were visible beginning June 10. Within the plumes, both BrO and HCl (since August) were detected and airborne Multi-GAS measurements indicated that SO₂ formed >99% of total sulfur (H₂S + SO₂) (Hidalgo et al., 2016). Seismic activity generally decreased during the initial weeks of June and remained at a lower level, although still above background, throughout July and the first 2 weeks of August. Additionally, a green colored lake appeared during the last weeks of July as reported by climbers. On August 14, a swarm of VT earthquakes (magnitude <2.7) preceded the first summit explosions by 12 h. These initial explosions occurred at 04:02 and 04:07 (UTM-

5), producing an ash and gas plume up to 8 km high. Fine ash fell on local communities to the northwest of the volcano covering over 500 km² (Bernard et al., 2016). On August 14, four subsequent ash emission events occurred, at 10:25, 13:45, 14:28 and 16:27. These explosions coincided with the emission of volcanic ash and strong gas emissions, with SO₂ release as high as 12,000 to 24,000 tons/day over the following week (Hidalgo et al., 2016). Four phases of ash emissions occurred between August and November, within which exist periods of high or periods of low ash emission (Fig. 2). The phases are: August 14 to August 15, August 15 to October 2, October 2 to November 4 and November 4 to November 30 (Phase 1, Phase 2, Phase 3 and Phase 4 respectively). The transition between Phase 1 and Phase 2 was marked by a change from explosive emissions during the first phase (defined by explosion seismic signals with associated infrasound signals) to passive emissions in the second phase (defined by the emission tremor seismic signals). During the second phase, almost four weeks of near continuous ash emissions occurred, where individual emissions lasted between an hour and >24 h at a time separated by hours of low level gas/ash emissions (Fig. 1B). The amount of ash in the plume dramatically reduced during the week beginning September 11, 2015, which coincided with a decrease in the emission tremor signal and an increase in VT event rate to 220 events per day (Fig. 2). SO₂ emission rates fluctuated significantly over this period, but remained relatively high, between 3000 and 10,000 tons/day. Multiple temperature measurements of the ash plume were taken with an IR camera over the course of the second eruptive phase with a maximum of 200 °C recorded on September 5. A third phase of lower intensity, intermittent ash emissions began on October 4, 2015 after a four week period of high VT seismicity rates. Intermittent, discrete explosions occurred over this period but were not associated with any significantly high-volume ash emissions. A fourth phase of low level ash emissions occurred during November 4–30, 2015, which produced a much smaller amount of ash and small transient events (Bernard et al., 2016). As of the start of 2016, surface activity was mostly limited to the emission of gas and water vapor, although VT seismicity rates remained high. The last ash emission was observed on January 24 but did not leave an observable deposit. The total volume of ash produced by this series of activity is 8.6×10^5 m³ (Bernard et al., 2016).

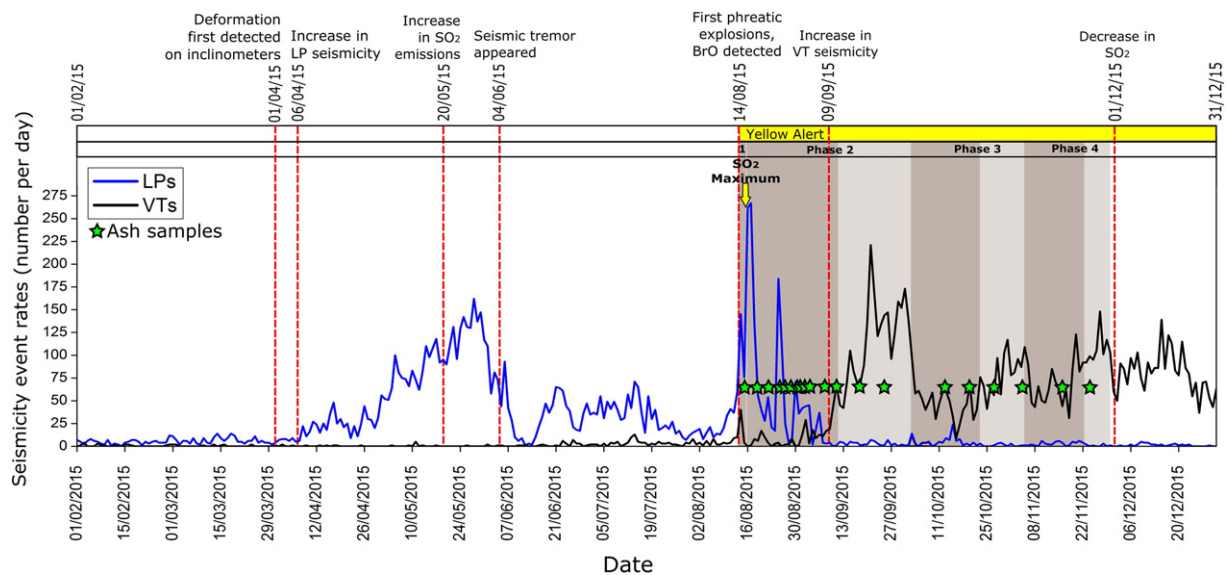


Fig. 2. Time line of events. Daily LP and VT seismicity event rates recorded by the seismic monitoring network of the Instituto Geofísico on Cotopaxi. Grey shaded areas show the 4 phases of ash emissions after the initial explosion on the morning of August 14 (the dark grey represents the period of high emissions and the light grey the period of low emissions within the phase) and the yellow arrow indicates the maximum SO₂ emission during this period of unrest. Red dashed lines indicate important changes in geophysical monitoring parameters and are indicated in the text. The green stars denote the sample collection dates.

3. Sample collection and methodology

The transport of volcanic ash is dependent upon atmospheric conditions, especially wind speed and direction. Atmospheric transport of ash introduces a sorting effect (e.g., through size and density differences), and sampling of distal ash can introduce large errors into analyses due to the removal of different components (e.g., Eychenne et al., 2013). In order to ensure that the analysis of ash is as accurate as possible, it is important to choose a sampling site close enough to the volcano and within the main deposition axis to reduce any sorting effects. BNAS is a seismic station (maintained by the IG) located on the western flank of the volcano, approximately six kilometers from the summit (Fig. 3A). Between August and December, a cumulative mass of 18,800 g/m² of ash fell at BNAS station (Fig. 3C). By comparison, the sampling sites BREF, located only 3 km from the crater on the north flank, and San

Elias, located 11.5 km from the crater in the southwest flank accumulated 200 g/m² and <100 g/m² respectively (Fig. 3C). The proximity of BNAS to the summit and its position directly under the main axis of the ash plume makes it an ideal sampling site to minimize the effects of density sorting in the plume. Samples of ash were collected every two to four days throughout the first four weeks of activity (14/08/2015–11/09/2015) from a solar panel at BNAS monitoring station. A total of 11 samples were collected during this period (Table 1). On August 26, an ashmeter (cf., Bernard, 2013) was installed at BNAS seismic station to more accurately collect and monitor the quantity and character of ash emitted (Fig. 3B). Ash collected with the ashmeters is representative of approximately 1 week of ash fall. During the latter portion of Phase 2 there was a three-week period of low ash emissions (12/09/2015–02/10/2015), during which two samples were collected from the ashmeter. During Phase 3 (2/10/2015 to 4/11/2015) four

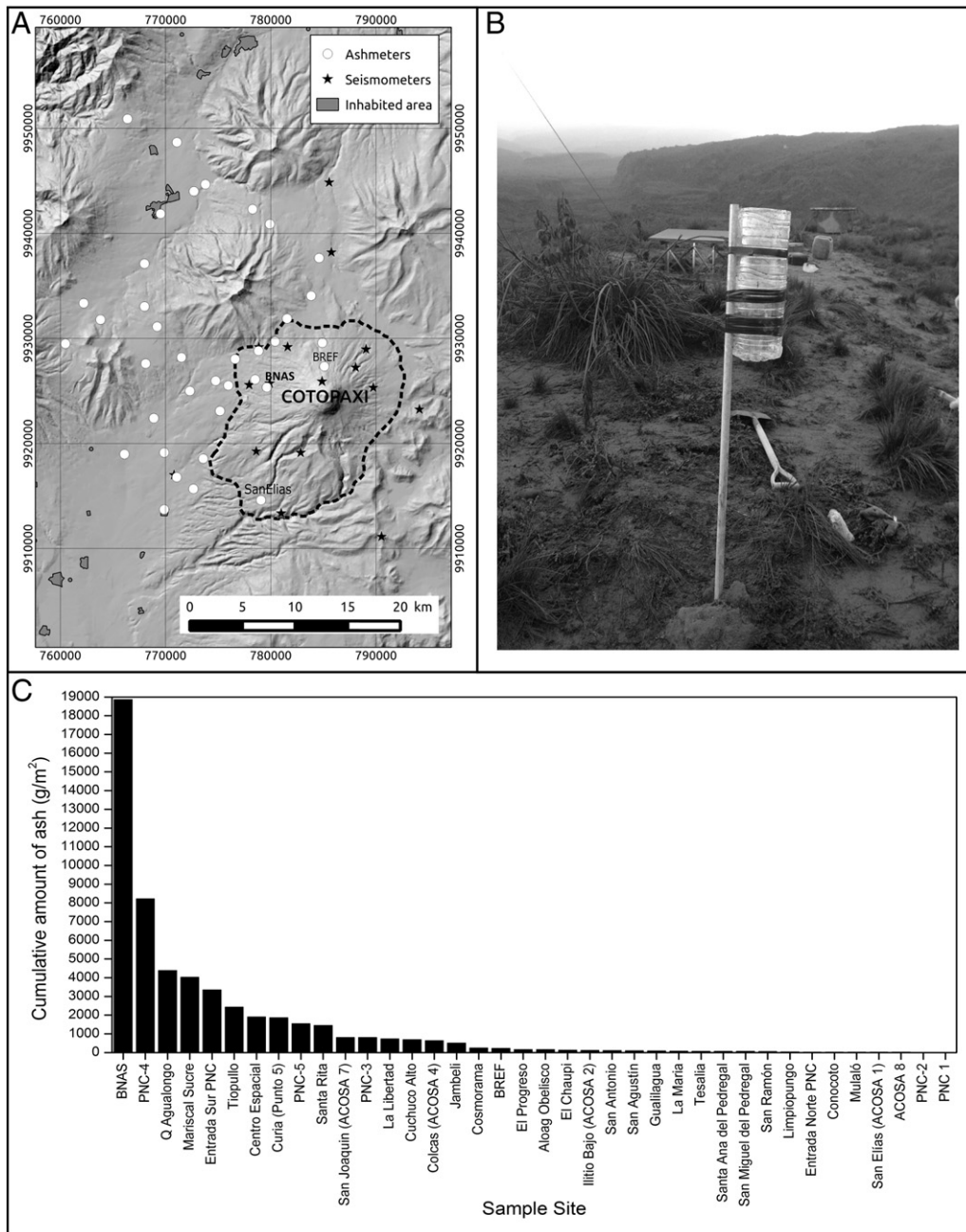


Fig. 3. (A) Location map of Cotopaxi with the seismic and ashmeter networks. BNAS (west), BREF (north) and San Elisa (south) are labeled on the image. The dashed line represents the extent of Cotopaxi Volcano. (B) Photograph of the ashmeter at BNAS taken on 26/08/15 after its installation. (C) Cumulative ash fall collected at each sample site between August 14 and the end of November 2015.

Table 1

Ash sample details. The date corresponds to the date the sample was collected (except where indicated with a * where a fresh sample was collected while scientists were on site). The samples were either collected from the solar panel or the ashmeter. The percentage of glassy with hydrothermal material is shown as a percentage of the juvenile component of each sample.

Emission phase number	Sampling data						Component classification				
	Sample number	Sample date	Sampling condition	Ash load (g/m ²)	Mean grain size Mz (Phi)	Sorting sigma-I (Phi)	Hydrothermal (%)	Lithics (%)	Free crystals (%)	Juvenile (%)	Glassy with hydrothermal (%)
Phase 1	NASA-1	15/08/15	Solar panel	176	4.62	1.99	47	27	2	24	4
	NASA-2	19/08/15*	Solar panel	87	5.32	1.82	39	17	18	26	3
Phase 2 high emissions	NASA-3	21/08/15	Solar panel	205	2.95	1.89	30	21	18	31	4
	NASA-4	24/08/15	Solar panel	1710	–	–	17	19	4	60	0
	NASA-5	26/08/15*	Solar panel	3255	–	–	11	12	4	73	0
	NASA-6	28/08/15	Ashmeter	2110	3.98	1.92	16	23	3	57	0
	NASA-7	30/08/15	Solar panel	238	–	–	10	14	3	72	0
	NASA-8	31/08/15	Solar panel	564	4.73	2.05	17	15	3	65	0
	NASA-9	02/09/15	Solar panel	1129	4.82	2.10	–	–	–	–	0
	NASA-10	04/09/15	Solar panel	71	4.37	1.97	–	–	–	–	0
	NASA-11	08/09/15	Solar panel	627	4.58	2.00	12	23	3	62	0
	NASA-12	11/09/15	Ashmeter	1838	4.57	2.09	4	10	2	84	0
Phase 2 low emissions	NASA-13	18/09/15	Ashmeter	229	2.90	0.98	–	–	–	–	0
	NASA-14	25/09/15	Ashmeter	351	3.63	1.47	–	–	–	–	0
Phase 3 high emissions	NASA-15	13/10/15	Ashmeter	807	4.13	1.94	11	15	6	68	0
	NASA-16	20/10/15	Ashmeter	3497	4.70	2.18	8	21	5	66	0
Phase 3 low emissions	NASA-17	27/10/15	Ashmeter	121	–	–	–	–	–	–	0
	NASA-18	04/11/15	Ashmeter	31	–	–	–	–	–	–	0
Phase 4	NASA-19	16/11/15	Ashmeter	94	–	–	–	–	–	–	0
	NASA-20	23/11/15	Ashmeter	202	3.15	1.26	15	15	4	66	0

samples were collected from the ashmeter, two samples during the first two weeks of high ash emissions and two during the following two weeks of low emissions. During Phase 4 of ash emissions (4/11/2015–30/11/2015), two samples were collected from the ashmeter. In total, 20 samples were collected from eruptions from August 14 to November 23, 2015.

Once collected, the ash samples were first dried in an oven overnight at 40 °C and then half the amount of each of the samples was sieved manually to 63 µm (in half-phi) in order to determine grain size distribution and to compare components among a consistent size fraction. The nominally sub-63 µm fraction was analyzed by laser diffraction at the Ludwig-Maximilians-Universität (LMU) Munich, Germany. 2–3 aliquots of approx. 0.1 g were measured for each sample in a Coulter LS230 to ensure reproducibility. For small samples (<5 g of ash), the whole aliquot was sieved and then analyzed. Grain-size distributions of 14 samples were obtained by combining manual sieving at a 0.5-Φ intervals ($\Phi = -\log_2 d$, where d is the particle diameter in millimeters) from -2 to 4Φ (4 mm–63 µm) and laser diffraction analysis for particles of $>3.5 \Phi$, such that both analytical techniques analyze the fraction between 3.5 and 4Φ (90 and 63 µm) following the methodology presented in Eychenne et al. (2012). The grains between 355 and 500 µm in size were selected for component analysis because this size range commonly contains >300 grains and this size is large enough to allow rapid identification of the different components. These grains were washed in water and cleaned in an ultrasonic cleaning bath to remove the fine ash coating. The cleaned grains were then dried in the oven at 40 °C for an additional day. Grains were then examined under a stereoscopic microscope and classified into one of four different lithologies, as described and characterized below. Where available, a minimum of 300 grains were classified to ensure a representative sample of the ash. For the samples that did not contain the minimum number of 300 grains of this size, the results were omitted from the componentry analysis due to large analytical error (SEM analysis was still performed on these samples) (Table 1). For SEM imaging, grains >125 µm in size were cleaned in water in an ultrasonic cleaning bath, and dried again. A selection of these grains was mounted on carbon tape and sputter coated with gold to image surface textures using a Vega Tescan scanning electron microscope in the Departamento de Metalurgia Extractiva (DMEX) in the Escuela Politecnica Nacional in Quito; other grains were mounted in epoxy mounts and ground flat, and polished in

order to document the internal textures of vesicles and crystals within ash grains at the U.S. Geological Survey (USGS) Cascades Volcano Observatory. Electron microprobe analyses were performed using the JEOL 8900 electron microprobe at the USGS, Menlo Park, California. A 15-keV, 8-nA electron beam with a 3 µm spot size was used to analyze glass compositions; Na and Si were analyzed first to minimize the effects of Na-loss.

4. Ash componentry classification

We analyzed 13 samples of ash (Table 1) using a stereoscopic optical microscope. Seven other samples were also analyzed but either did not contain enough grains of the target size after sieving (e.g., extremely fine-grained ash from the 02/09/2015) or total sample size was too small (Table 1). We first classified the ash grains into four groups based on grain lithology and morphology: hydrothermal/altered grains, lithic fragments, juvenile material, and free crystals (Fig. 4). Hydrothermal grains were classified based on their color and luster (including metallic luster, sulfide minerals, white color characteristic of gypsum and quartz, and red color of oxidized glass), and/or the presence of mineral deposits on the surface of the grains or within the vesicles of scoriaceous grains. Lithic fragments were classified according to their dull, opaque but unaltered appearance. Juvenile fragments were classified according to their black or dark grey color but more importantly, their glossy appearance and sometimes semi-vesicular nature. Free crystals consist of individual phenocrysts (here, phenocrysts are used to distinguish crystals based on size alone) or fragments of crystals of different minerals containing <10% adhering groundmass material.

5. Petrological and granulometric characteristics

5.1. Surface and microlite textures

Each particle type contains distinct textural and mineralogical associations between microlite and phenocryst phases, where crystal components common to most ash grains include a combination of plagioclase, pyroxene, and oxide phases, and sparse glass between microlites (crystals <40 µm in size).

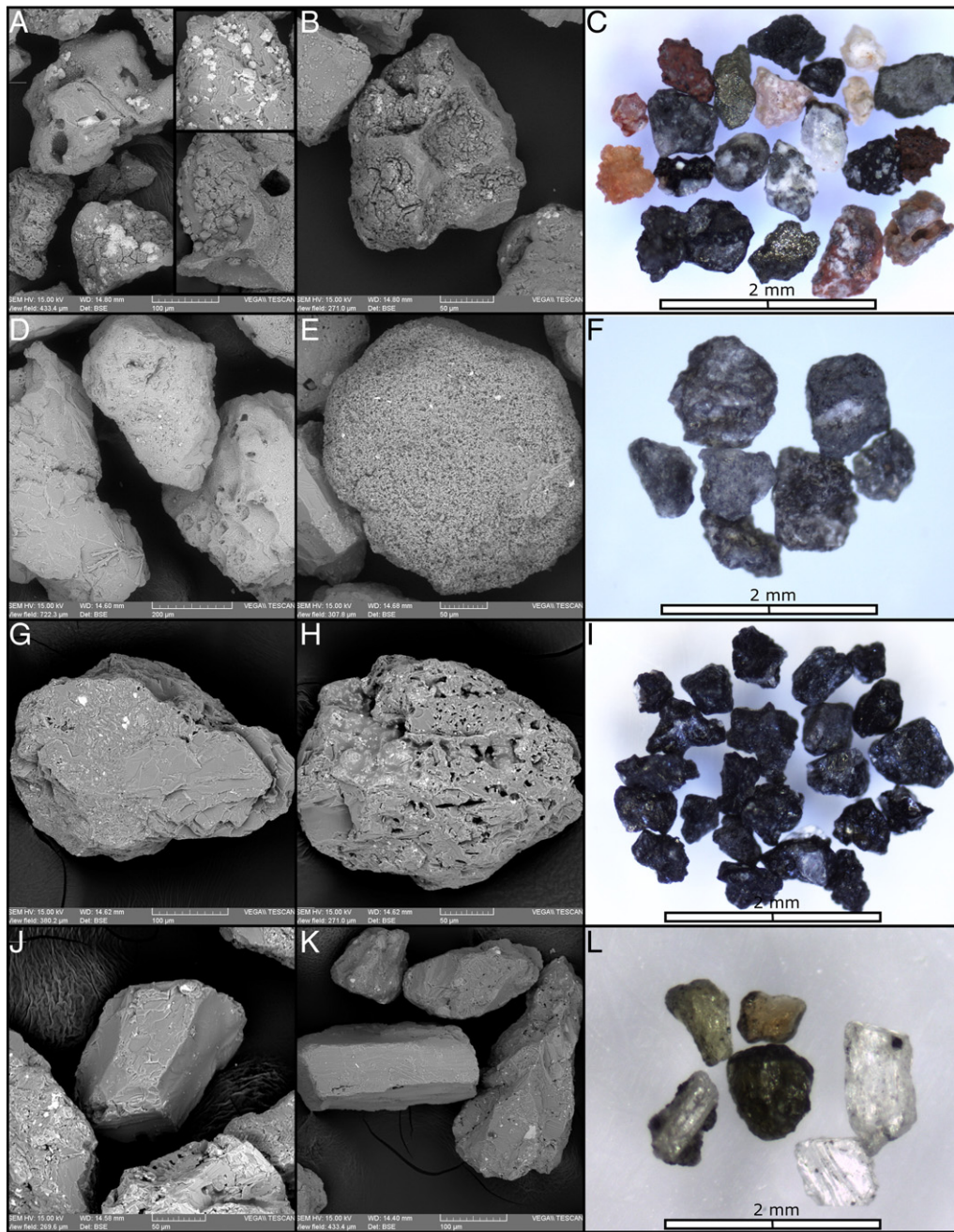


Fig. 4. SEM backscatter photomicrographs and stereoscope images of the different classified components of the Cotopaxi ash samples: hydrothermal material (A, B and C), lithics (D, E and F), juvenile (G, H and I) and free crystals (J, K and L). Altered surfaces (A), pyrite crystals (A inset top and C), cubic quartz (A inset bottom) and infilled vesicles (B) are apparent in the majority of grains along with red and orange oxidation of the grains (C). Pitted and worn surface of lithic fragments are apparent (D), while some are holocrystalline and rounded (E). Fresh fractures in highly microcrystalline grains (G) are present and also residual glass between microlite grains of the juvenile grains (H) with black vitreous fresh surfaces (I). Free crystals retain their euhedral shapes (J and K).

5.1.1. Hydrothermal/altered material

Clasts classified as hydrothermal material are characterized by surface alteration and oxidation, producing a red to rusty color and/or are covered by secondary mineral precipitates white to metallic in color and luster (Fig. 4A, B and C). The grains have a wide range in particle morphology, including irregular angular to sub-angular shape as well as rounded varieties. Particles span a range of vesicularities from non-vesicular to moderately vesicular based on the values from Houghton and Wilson (1989). Vesicular scoriaceous particles commonly contain secondary precipitates on outer surfaces and within pore space (Fig. 4B). Secondary precipitates include acicular gypsum needles

(Fig. 4D), abundant free or surface-coating sulfides (Fig. 4A inset and C), and white or opaque hydrothermal quartz (vuggy quartz) (Fig. 4C). In gas-rich plumes, secondary phases can condense on solid particles very quickly (Ayris et al., 2013), so extra care has to be devoted to avoid misinterpretation.

Hydrothermally altered and oxidized grains are the most petrologically diverse. Grains contain abundant opal, alunite, pyrite, and sparse cristobalite and primary magmatic phases that include plagioclase, pyroxene (clinopyroxene and orthopyroxene), and magnetite (Fig. 5A–C). In some cases, alunite fills pore space, in others it forms large portions of ash grains (Fig. 5A) and pyrite coats grain surfaces (Fig. 5B).

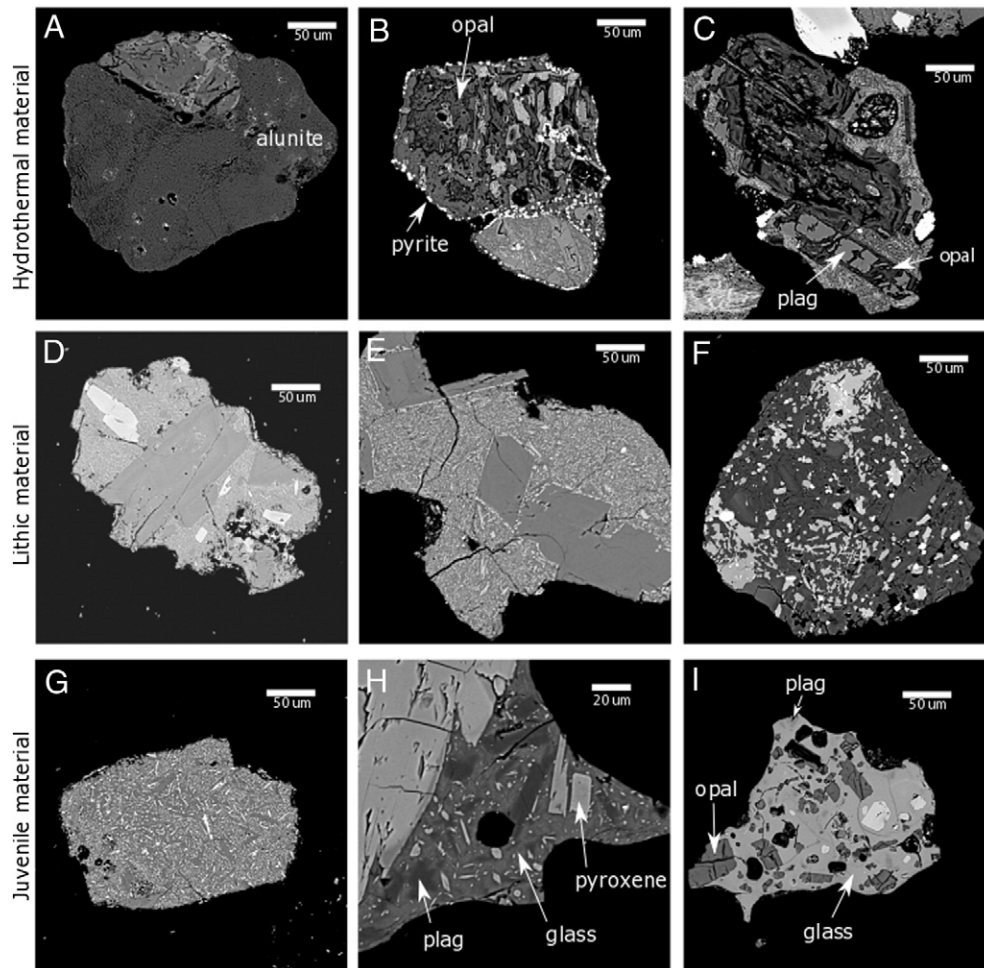


Fig. 5. Backscattered electron images of (A–C) hydrothermally altered grains. (A) Alunite (dark grey) covers the bottom half of this grain, opal has replaced plagioclase microlites; (B) pyrite crystals (white) coat the surface of this grain that surrounds opal (dark grey), plagioclase (light grey) and crystalline groundmass; (C) opal replaced plagioclase microlites (see original plagioclase core at image bottom); (D–F) lithic grains: note the abundance of microlites in the groundmass and the lack of visible fresh glass (E) mafic microlites are concentrated along plagioclase crystal margins; (G–I) juvenile grains including: (G) highly microcrystalline grain containing fresh glass interstitial between tabular microlites <30 µm in length; (H) moderately microcrystalline grain containing plagioclase and orthopyroxene in a glassy groundmass; (I) low micro-crystallinity ash grain containing opal xenocrysts (dark grey), and pyroxene and plagioclase microlites (white and light grey).

Opal commonly replaces plagioclase (Fig. 5C) and pyroxene. Groundmass in these grains is completely or nearly completely devitrified, crystalline, or replaced (Fig. 5C).

5.1.2. Grey lithics

Most commonly, the lithic fragments consist of grey to black lava fragments with dull, opaque, pitted surfaces (Fig. 4D, E and F). These grains vary from blocky to very irregular in shape. These fragments display a range of internal textures, but generally lack hydrothermal alteration phases. Many lithic grains contain abundant microlites with tabular pyroxene crystals most commonly measuring between 10 and 25 µm (Fig. 5D–F). Fresh glass is not visible between microlites in these grains.

5.1.3. Juvenile grains

Juvenile grains are distinguished primarily based on their glossy surface texture, unaltered, fresh surfaces, and the presence of fresh glass. These grains have two distinct morphologies, blocky, and porous. The blocky grains have sub-planar faces and consist of dense clasts with varying microlite contents and large phenocrysts (Figs. 4H; 5H; 6C), and in some cases contain large vesicles with thick interstitial groundmass septa (Figs. 4H; 5H and I). These dense grains commonly exhibit trans-granular and grain boundary micro-fractures with apertures of ~2 µm (Fig. 6D). Blocky grains are commonly light grey to black in

color with a vitreous luster and contain variable amounts of microlites and fresh glass (Fig. 4I). The porous grains consist of diktytaxitic lattices of microlite crystals with varying amounts of interstitial glass (Fig. 4H and Fig. 6A and B), where pore space represents interstitial space between microlite crystals rather than vesicles (Fig. 6A and B).

The groundmass glass content of juvenile clasts is variable (Fig. 4H), where microlite networks are present to varying degrees. Juvenile grains contain the smallest microlite crystals and the greatest proportion of fresh glass of all grain types. The grains that contain the most glass contain feldspar microlites surrounded by fresh glass, but in some grains also contain opalized feldspar that lacks reaction rims or alteration halos (Fig. 5I) and are completely surrounded by fresh glass. Alunite is also present within very few of these grains. Opal and alunite are hydrothermal alteration minerals; however, in contrast with the extensively altered, crystalline, or devitrified groundmass that is associated with the opal and alunite in hydrothermal grains (Fig. 5A–C), the glass in juvenile grains is pristine. In the most crystalline clasts, pyroxene microlites are generally smaller than in clasts in the lithic category (Fig. 5G vs. I), measuring between <1 and 20 µm, and commonly surrounding phenocrysts of plagioclase (Fig. 5), but textures of the most crystalline grains in this class overlap with the finest microlite-rich lithic grains. Some grains also contain fresh glass interstitial between microlites; those microlites include plagioclase and pyroxene (Fig. 5H), and also include opal (Fig. 5I).

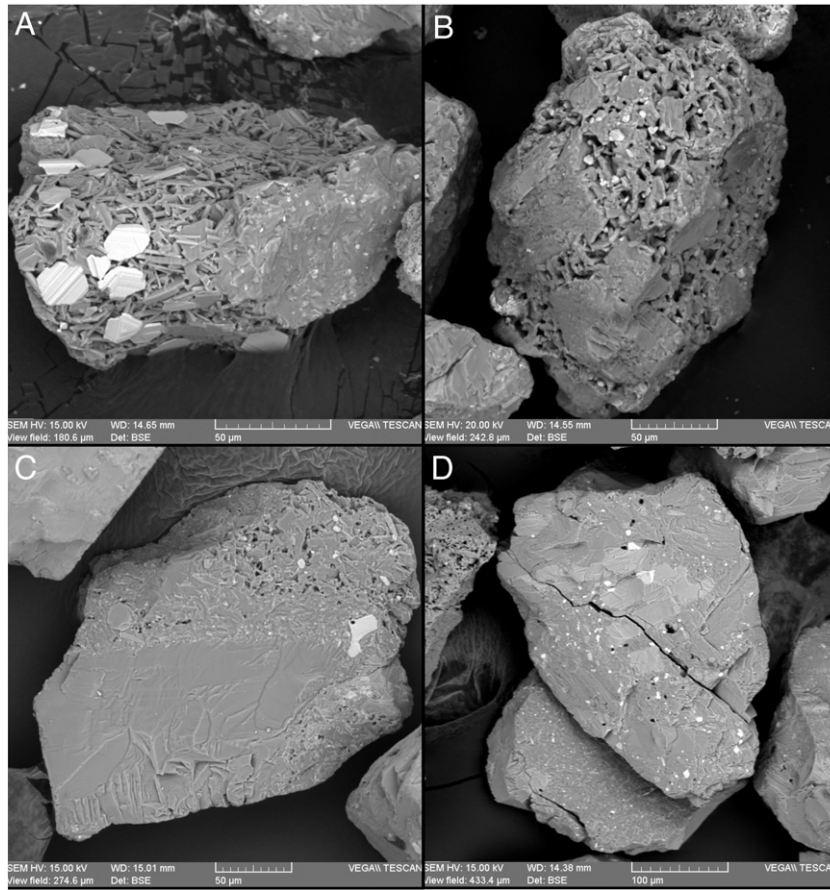


Fig. 6. SEM backscatter photomicrographs of ash grains of important ash textures. (A and B) Ash grains showing diktytaxitic textures (disorganized lattices of plagioclase, pyroxene and Fe-Ti oxide crystals with varying amounts of interstitial glass). (C) Blocky planar-edged grain containing a large plagioclase phenocryst surrounded by microlite. (D) Dense microlite-rich grain containing a thermal fracture.

5.1.4. Free crystals

Free crystals are generally large phenocrysts of plagioclase, with lesser amounts of pyroxene (Fig. 4J, K and L). Crystals are generally intact and retain their crystal form and commonly have adhering ground-mass material. Fragments of free crystals are also present.

5.2. Glass compositions

Glass compositions from five analyzed juvenile ash grains have dacitic compositions (Table 2). The greatest abundance of glassy ash grains occurs in the earliest erupted sample (juvenile grains from later emissions are microlite rich and have a low glass content), August 15,

2015. The glass rich grains with hydrothermal minerals represent approximately 4% of the total volume of juvenile ash particles in the samples from the first explosions (Table 1). Glass is fresh, analytical totals range from 96.8–98.6 wt%; anhydrous glass compositions range from 63.4–66.4 wt% SiO₂ and 7.2–7.9 wt% FeO (Fig. 7). Glass compositions were analyzed from two ash grains in the hydrothermal category and have 65.1 and 77 wt% SiO₂, with FeO and Na₂O contents distinct from those of glass in juvenile grains (Table 2).

5.3. Grain size distributions

Grain-size distributions of 14 samples were obtained by combining manual sieving and laser diffraction analysis. The grain size fraction

Table 2
Anhydrous glass compositions of erupted ash grains from Cotopaxi, 2015.

Sample details		Glass chemistry (wt%)											
Sample date and grain designation	# of analyses	SiO ₂	TiO ₂	Al ₂ O ₃	FeO	MnO	MgO	CaO	Na ₂ O	K ₂ O	Cl	P ₂ O ₅	Unnormalized total
<i>Juvenile</i>													
15 August 2015 B1	9	63.6	1.3	14.3	7.4	0.2	1.6	4.3	3.2	3.5	0.09	0.6	98.65
15 August 2015 B3	5	66.4	1.2	13.5	7.6	0.1	1.1	2.5	3.9	3.0	0.08	0.6	96.82
15 August 2015 XL	3	63.4	1.3	14.1	7.9	0.1	1.6	4.3	3.5	3.1	0.16	0.6	97.00
15 August 2015 BW2	9	64.2	1.3	14.5	6.7	0.0	1.9	4.4	3.8	2.6			97.52
15 August 2015 BW3	6	64.2	1.2	14.3	7.2	0.2	1.9	4.9	3.3	2.1	0.04	0.6	96.88
15 August 2015 BW4	9	64.7	1.2	14.5	7.6	0.1	1.6	4.0	3.3	2.3	0.10	0.6	97.12
15 August 2015 BW6	10	65.8	1.3	13.7	6.2	0.0	1.6	3.5	2.5	4.9			97.70
<i>Hydrothermal</i>													
15 August 2015 W1	3	77.0	1.0	13.7	3.4	0.0	0.1	0.6	0.4	3.5	0.2	0.2	93.48
15 August 2015 P2	5	65.1	0.0	23.9	0.9	0.0	0.0	6.4	6.9	0.9			97.70

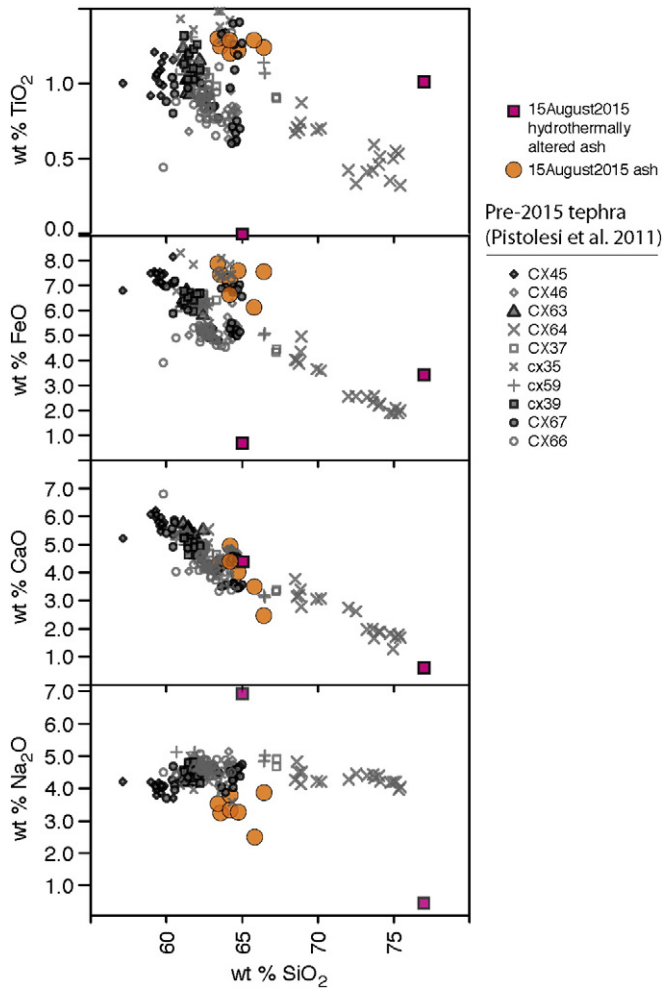


Fig. 7. Glass compositions of juvenile grains and hydrothermally altered grains in 2015 ash samples superimposed on glass compositions of Holocene pyroclasts from Cotopaxi of Pistolesi et al. (2011).

between -1 and -2Φ ($2-4$ mm), which corresponds to fine lapilli (White and Houghton, 2006), was measurable only in the 15/08 sample (0.3 wt%). In comparison with other volcanic ash, the ash emitted by Cotopaxi volcano is fine to extremely fine-grained with moderate to poor sorting and positive skewness. Most of the Cotopaxi ash grain-size distributions are bimodal with a sharp coarse mode (0.0 to 3.7 Φ) and a flat fine mode (4.0 to 6.3 Φ) (Fig. 8). Interestingly, the grain-size mean and median are largely controlled by the proportion of coarse and fine mode rather than by their absolute value. There is not a clear evolution through time, but the grain-size distribution is generally finer during the heaviest ash falls (14–15/08; 28/08–11/09; 13–20/10) whereas the smallest volume ash deposits (21/08; 18–25/09; 23/11) have coarser distributions, potentially resulting from wind reworking of the fine-grained material.

6. Temporal variation of ash componentry

The componentry of ash samples changed through time (Figs. 4, 9, 10 and Supplementary Fig. 2). Proportionally, ash from the initial explosions on August 14 is dominated by lithic fragments and hydrothermal material (27% and 47% respectively; Fig. 9). Free crystals and juvenile fragments make up only a relatively small percentage of that sample (26% combined). Further, although a portion of the free crystals may be derived from the juvenile melt, they cannot all be considered as such. During the first 10 days of the eruption, the percentage of juvenile grains increased up to 60%, whereas the percentage of hydrothermal

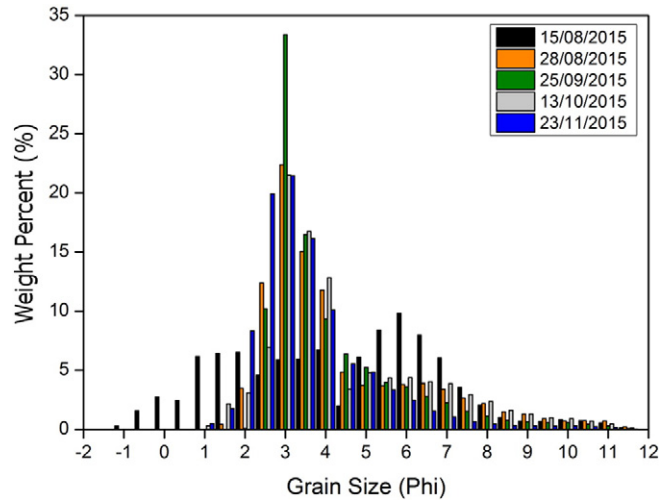


Fig. 8. Grain-size distribution of five ash samples from the Cotopaxi eruption (in half- Φ interval). Note that most samples show bimodal distribution with a sharp coarse mode ($\sim 3 \Phi$) and a flat fine mode. Distributions are positively skewed and platikurtic to mesokurtic. Full data on the grain size distribution is shown in the supplementary material 1.

material and lithic grains significantly decreased (to 17 and 19%, respectively) (Fig. 9). The relative abundance of hydrothermal material continued to decrease to $<16\%$ where it remained throughout the rest of Phase 2, whereas the percentage of juvenile material continued to increase (Fig. 9) with some small fluctuations. Furthermore, the textures of juvenile grains changed through time. Early-erupted juvenile grains had lower microlite crystallinities than those in late eruptions (Fig. 10). The third phase of emissions began in the week of the October 4. Samples from the third phase of emissions contained between 66 and 68% juvenile grains, whereas the free crystal content remained $<6\%$, hydrothermal $<15\%$ and lithics $<24\%$. This trend continued throughout the rest of the eruptive events, where the juvenile material consistently stayed $>65\%$. The lithic content, hydrothermal material and free crystals

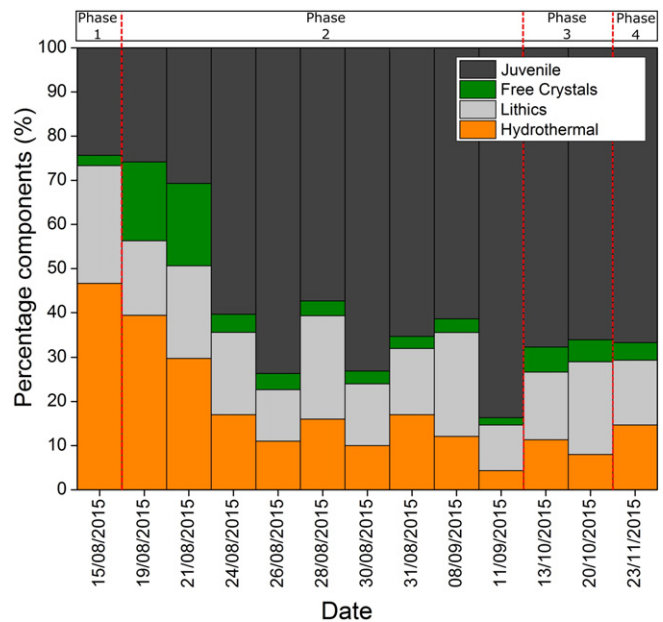
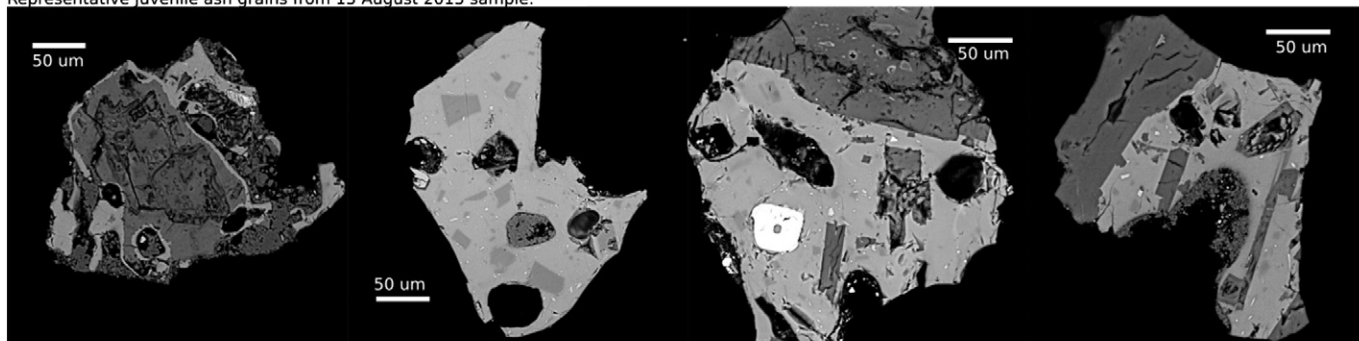


Fig. 9. Ash componentry histogram. Percentage of hydrothermal, lithics, free crystal and juvenile grains in 13 samples of ash. 7 other samples were analyzed but there was not a sufficient number of grains for representative analysis and so these results have been omitted.

Representative juvenile ash grains from 15 August 2015 sample:



Representative juvenile ash grains from post-15 August 2015 samples:

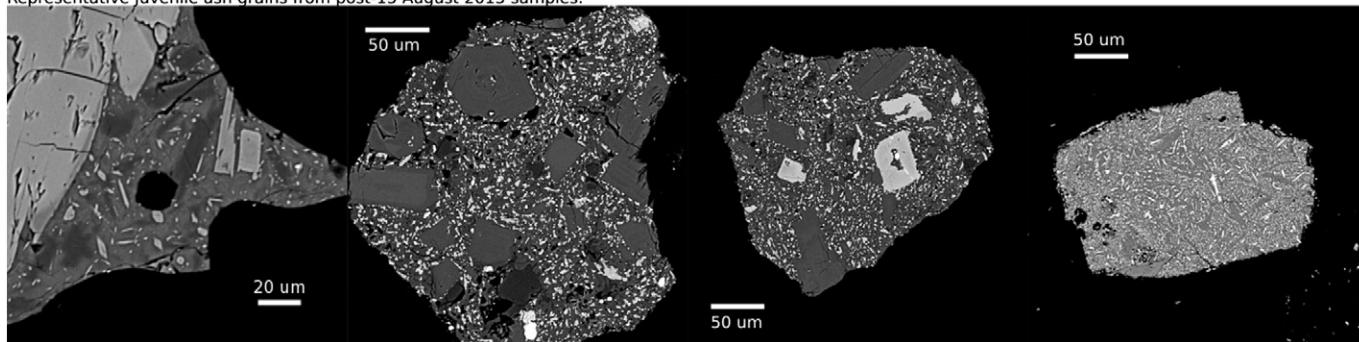


Fig. 10. Backscatter SEM images of polished sections showing the evolution of the texture and crystallinity of the juvenile grains.

remained relatively constant throughout emissions through the end of November 2015.

7. Eruption dynamics and the recognition of juvenile magma

The renewed eruption of Cotopaxi provides a unique opportunity to study the temporal evolution of ash through the reawakening of a large stratovolcano after a long period of quiescence.

7.1. Phase 1

Samples of ash from the first week of the eruption were rich in lithics, hydrothermally altered grains and oxidized lithic material (Figs. 4C and 9). During hydrothermal alteration, secondary phases (e.g. alunite) are crystallizing in pore space or replace groundmass glass or minerals that are decomposed. This pervasive rock alteration can significantly affect appearance and mechanical properties (Mayer et al., 2016). Red, altered components were classified ‘oxidized lithics’ by Pistolessi et al. (2011) in their analysis of Cotopaxi eruptive products over the past 800 years. These samples are representative of material that filled the conduit that was cleared out in the “vent-clearing” phase. During this initial eruption, the abundance of juvenile material is small, however, juvenile grains contain more glass than later in the eruptive sequence (Fig. 10). Electron microprobe analyses of glass are consistent with lack of alteration based on high analytical totals. Furthermore, glass compositions are consistent with that expected at Cotopaxi. Fig. 7 shows glass compositions from a variety of previous tephra units from Cotopaxi; glass compositions of ash grains in this study have compositions overlapping with previous eruptive units (Pistolessi et al., 2011). In contrast, glass compositions from hydrothermally altered components have distinct compositions (Fig. 7). The most compositionally similar tephra unit of Pistolessi et al. (2011) is that erupted in small volume explosions that occurred post-1880. The presence of these abundant clasts with unaltered glass, and their decreasing abundance in ash samples through time provides strong evidence that these grains are fresh, juvenile magma.

Changes in the crystallinity of the juvenile material results from changing ascent and decompression conditions within the conduit (e.g., Hammer et al., 1999). By comparison with experiments and with ash studies of historic eruptions elsewhere, the presence of glassy ash grains, with low micro-crystallinities as was observed most abundantly (but still a minor portion of the eruptive material, Figs. 5I, 7) in the August 15 sample, suggests relatively rapid ascent of juvenile magma, fast enough to suppress or mostly prohibit extensive microlite crystallization. The increasing percentage of juvenile magma fragments in the ash as the eruption progressed and the decreasing content of “old” material suggests a progressive increase in the relative involvement of the magmatic system. The initial explosions and emission phase over the first two days are therefore interpreted as hydro-magmatic when the rising magma served primarily as a heat source that disturbed the fragile equilibrium of the hydrothermal system (Mayer et al., 2016). As such, the ejected ash is primarily comprised of lithics with variable degrees of hydrothermal alteration (including hydrous opal and alunite phases) and only minor clasts of fresh juvenile melt (Figs. 5 and 10). The small amount of juvenile material containing hydrothermal minerals in samples from August 15 preserve evidence for magma intrusion into the hydrothermal system, providing a trigger for the initial hydro-magmatic explosions.

7.2. Phases 2–4

After the first two weeks of eruptions (14–30/08/2016), which saw the highest ash emission rates (Bernard et al., 2016), the relative proportion of hydrothermal-altered and oxidized fragments decreased, which is interpreted to represent clearing of the magma ascent path, and reduction in interaction with the host country rock. Over the same interval, the proportion of microlite-rich, blocky fragments in the juvenile component increased. As the eruption sequence continued, these juvenile grains transitioned to higher micro-crystallinity material (Fig. 5G and H; Fig. 10) due to slower ascent and/or longer residence times at shallow levels, as would be expected in a dome or a shallow conduit plug (e.g., Nakada and Motomura, 1999; Hammer et al., 1999;

Hammer and Rutherford, 2002; Cashman and Hoblitt, 2004). Highly crystalline juvenile material has been documented in ash samples at several other volcanoes. For example, coarsely vesicular clasts from 2010 Eyjafjallajökull eruptions reached 55% micro-crystallinity (Cioni et al., 2014); blast deposits from Mount St. Helens in 1980 reached 62% (Cashman and Hoblitt, 2004); and eruptive products from Colima 1913 and May 2005 eruptions reached ~80% and ~90% micro-crystallinities, respectively (Savov et al., 2008). The increase in crystallinity of the juvenile fragments during the second phase of the eruption (Fig. 10) alludes to a progressive rheological stiffening of the magma which would lead to increasingly lower ascent rates and the formation of shallow plug (e.g., Sparks, 1997 and Cordonnier et al., 2012).

During the second phase of ash emissions, grains with a diktytaxitic textures (Fig. 6A and B) and varying amounts of residual glass appeared and began to increase in abundance. One mechanism for the formation of diktytaxitic textures in andesite magmas is gas driven filter-pressing, where a gradient in gas pressure drives melt expulsion from a crystal lattice (e.g., Sisson and Bacon, 1999; Pistone et al., 2015, Kushnir et al., 2016). Here, we infer that this process has occurred to varying degrees within the conduit of Cotopaxi, resulting in grains with varying amounts of residual glass/melt coating the lattices of microlite crystals. Further work into the nature of filter-pressing within the shallow plug is warranted, but is beyond the scope of this paper.

The fragmentation mechanisms responsible for the observed dense, microlite-rich pyroclasts emitted during continuous ash emissions have been somewhat enigmatic. In contrast to the first phase, the second through fourth eruptive phases were semi-continuous, low-energy ash venting phases and lacked high temperature plumes (max. recorded temperature of 200 °C). During overflights made by the IG after the August 14 explosions, it was observed that the crater lake present before August 14 had disappeared, suggesting that the availability of surface water had decreased. Although the large summit glacier remained on top of the edifice, magma interaction with water was reduced due to the thermal aureole that evolved around the magma column. The quasi-continuous ash emission may (partially) derive from discrete explosions but has been obscured by complex gas-and-ash ascent processes in the conduit following explosions several hundreds of meters down in the volcanic edifice. The fine grain size distributions of all ash samples suggest that the fragmentation mechanism was very efficient (Kueppers et al., 2006) and its constancy may reflect similar fragmentation mechanisms throughout the ensuing period of continuous ash emissions. Due to the high proportion of highly dense microcrystalline juvenile material, we believe that continuous emissions resulted from the brittle fragmentation of a dense magma plug due to thermal and mechanical stresses and decompression (e.g. Ono et al., 1995; Taddeucci et al., 2002), although it is clear that water is still present in the edifice at Cotopaxi based on the nature of continuing shallow seismicity, including LF events (cf. Ruiz et al., 1998). We suggest that phases 2–4 represent repetitive formation and destruction of a shallow magmatic plug.

7.3. Geophysical evidence for juvenile magma intrusion

The origin of juvenile ash fragments includes two possibilities: (A) that the fragments represent unaltered past eruptive products from Cotopaxi, excavated from portions of the edifice that did not experience hydrothermal alteration, vapor-phase alteration from the extensive degassing prior to August 14, or oxidation; or (B) that the fragments represent juvenile magma that initially ascended and interacted with the hydrothermal system, producing the first explosions, then progressively degassed and crystallized in response to slowing ascent rates or increasing shallow residence and shallow degassing prior to eruption. Distinction between the possibilities requires a holistic view of the system and comparison with past eruptive products from Cotopaxi.

Several different monitoring parameters support interpretation B, a shallow magma intrusion and degassing at Cotopaxi in 2015. Magmatic degassing at Cotopaxi has been close to the detection limit for DOAS techniques over the past several years; background rates of SO₂ emission were below 100 tons/day since permanent DOAS instruments were installed in 2008. SO₂ emission increased in May, remaining high through eruptive/explosive events in August–November. Furthermore, BrO was clearly detected in the plume since August 14 (Dinger et al., 2016), indicating magmatic degassing through a dry pathway (cf., Bobrowski et al., 2003). Moreover, measurements of high SO₂/H₂S ratios support an interpretation of magmatic degassing rather than of a hydrothermal origin. Additionally, no broad deformation was detected via InSAR techniques, however minor deformation (≤ 1.5 cm) was detected with the GPS and tiltmeter network, consistent with possible minor inflation of the edifice. An observed orange glow within the crater for several days since October 02 also requires elevated (magmatic) temperatures at the surface. Finally, seismic patterns are consistent with shallow magma residence, including abundant low frequency seismicity and later VT seismicity (Fig. 2). LP and VT seismicity during this period were substantially elevated above previous levels of monitored unrest at Cotopaxi possibly resulting from the intrusion and interaction of shallow hot material (e.g., magma) with water (e.g., in the hydrothermal system; Ruiz et al., 1998). During the 3rd and 4th phases there was a clear increase in small transient seismo-acoustic signals (Bernard et al., 2016), coincident with the observed orange glow in the crater and consistent with the repeated formation and destruction of a shallow magmatic plug. The observational evidence for shallow magma ascent (to less than approximately 3 km depth based on seismicity) by August 2015 is abundant. This evidence combined with the appearance of fresh glass that contains few microlites in the earliest erupted ash and the more microlite-rich material erupted later in the sequence suggests the simplest explanation for componentry changes in ash produced from eruptions starting on August 14, 2015, is the ejection of juvenile magma that initially rose quickly but then stalled to form a shallow plug later in the episode.

7.4. Hazard assessment and future activity

Completely aphyric, glassy fragments are absent, indicating that no single eruption has tapped all the way down to the gas rich magma source region. Large volume past eruptions at Cotopaxi produced pyroclasts with glassy textures, as are common in the eruptive products from the VEI 4 eruption of 1877 (Pistolesi, pers. comm). The presence of ash grains that we now recognize as juvenile, with low crystal content and very finely micro-crystalline textures suggests that at least a semi-open pathway exists from the magma source to the surface. Pre-eruptive gas emissions indicate that magma was able to freely and effectively degas under “open-system” conditions, reducing the potential for a buildup of large, hazardous gas-overpressures (Woods and Koyaguchi, 1994). Instead, the juxtaposition of glassy groundmass with few microlites and hydrothermal minerals/fragments may indicate that initial eruptions were triggered by the interaction of magma with the hydrothermal system. The observations of increasingly abundant dense, microlite-rich juvenile ash grains, suggests slowing magma ascent rates and residence times sufficient to allow degassing and crystallization of the magma. Furthermore, elevated gas emissions have continued, suggesting that significant gas overpressures are not accumulating in the conduit, potentially decreasing the *short term* likelihood for a large explosive event (e.g., Eichelberger et al., 1986; Woods and Koyaguchi, 1994; Jaupart, 1998).

Alternatively, an open pathway to the surface may also allow a new batch of magma to ascend easily in the future (e.g., Scandone et al., 2007). It is also probable that not all the intruded magma was expelled during the emission phases and that the semi-open conduit that existed during the ash emission phases now contains a highly crystalline plug of degassed magma. In this case, future eruptive activity would require a

vent-clearing phase to allow the ascent or eruption of a new magmatic pulse. However, the dynamics of magmatic systems can rapidly change with little warning, resulting in a sudden large explosive eruption as happened at Reventador volcano in 2002 (e.g., Hall et al., 2004 and Samaniego et al., 2008). There, a swarm of VT, LP and tremor seismicity ~3 h prior to eruption was the only warning that a large eruption was about to occur. The eruption was interpreted to be phreatomagmatic based on the production of fine-grained angular ash fragments mixed with basement rock and old lavas (Samaniego et al., 2008). The paroxysmal phase of that eruption lasted ~45 min and generated at least five large pyroclastic flows that reached ~9 km east. As such, rapid changes can occur at volcanoes, therefore only through continued monitoring of the volcano (e.g., deformation, seismicity and gas) is it possible to detect changes in the magmatic system that could indicate changes in future activity.

8. Importance of ash analysis for volcanic monitoring at Cotopaxi

The near real-time analysis of ash samples from precursory explosive activity at Cotopaxi volcano during the months of August, September, October and November 2015 was used as a complementary aid to assist with the interpretation of the geophysical monitoring signals. Compositional and textural analysis provided invaluable information about the degree of involvement and the ascent conditions of the newly intruded magma body. The main findings of this paper are:

- Juvenile ash fragments are recognized in Cotopaxi ash based on the presence of unaltered glass containing few microlites. Microprobe analysis of the fresh glass shows high analytical totals and compositions consistent with previous eruptions at Cotopaxi, but unlike compositions of the groundmass in hydrothermal material.
- Juvenile material in the initial explosions (Phase 1) is glassy and contains opal in contact with fresh melt preserving evidence for interaction between magma and the hydrothermal system.
- The componentry of ash evolved from dominantly hydrothermal and lithic material to dominantly juvenile material through the 2015 eruptive sequence.
- The nature of juvenile clasts also changed through the eruptive sequence. The juvenile clasts found in the earliest erupted material are quasi aphyric. Later eruptions produced clasts with higher amounts of microlites.
- Increasingly high micro-crystallinities in the juvenile grains from phases 2–4 suggest slowing ascent rates and increasing duration of shallow storage in a system open to gas loss where fragmentation was a result of brittle breakage of a shallow magmatic plug.
- Grain size distributions show bimodal distributions but very little variation throughout the eruption suggesting the eruption dynamics do not change significantly.
- Geophysical signals (high LP and VT event rates, buried explosion signals, elevated SO₂ emissions, detection of BrO, high SO₂/H₂S ratios and inflation of the volcanoes flanks) support the conclusion of the involvement of juvenile magma.

Ash analysis in itself cannot and should not be used to inform forecasts about future activity, but can provide perspective about the ascent conditions and dynamics of erupted material. Accurate knowledge of past eruptions helps to constrain possible future eruption scenarios, especially for well-preserved large eruptions. At Cotopaxi in 2015, petrologic monitoring of ash grains was used to complement geophysical monitoring techniques. Based on these studies we conclude that there was new magma involved in ash emissions but that the ascent rate was slow and the system was open to continued gas outgassing and escape, which lowered the *short term* probability of a large explosive eruption. However, monitoring parameters are still above background at the

time of this writing, so the ultimate fate of this period of unrest still requires close monitoring of the volcano.

Supplementary data to this article can be found online at <http://dx.doi.org/10.1016/j.jvolgeores.2016.10.013>.

Acknowledgements

We would like to acknowledge all members of the Instituto Geofísico, especially those who were involved in the response to the volcanic crisis and who assisted with sample collection and analysis. The authors would like to thank John Pallister and the team from VDAF for insightful discussions, Leslie Hayden at the USGS Menlo Park for help with electron microprobe analyses, and members of DEMEX-EPN for their assistance with the SEM work. This research has been conducted in the context of the Laboratoire Mixte International “Séismes et Volcans dans les Andes du Nord” of IRD. This work is the contribution n°3 of the project “Grupo de Investigación sobre la Ceniza Volcánica en Ecuador”. U.K. acknowledges the support by grant KU2689/2-1 from the Deutsche Forschungsgemeinschaft and by the Marie Curie Initial Training Network “VERTIGO”, funded through the European Union Seventh Framework Programme (FP7 2007–2013) under Grant Agreement number 607905. Any use of trade, firm, or product names is for descriptive purposes only and does not imply endorsement by the U.S. Government.

References

- Ayriz PM, Lee AF, Wilson K, Kueppers U, Dingwell DB, Delmelle P. SO₂ sequestration in large volcanic eruptions: high-temperature scavenging by tephra. *Geochim. Cosmochim. Acta*, 110, June 1, 2013, 58–69, (ISSN 0016-7037)
- Barberi, F., Coltelli, M., Frullani, A., Rosi, M., Almeida, E., 1995. *Chronology and dispersal characteristics of recently (last 5000 years) erupted tephra of Cotopaxi (Ecuador): implications for long-term eruptive forecasting*. *J. Volcanol. Geotherm. Res.* 69 (3–4), 217–239.
- Bernard, B., 2013. *Homemade ashmeter: a low-cost, high-efficiency solution to improve tephra field-data collection for contemporary explosive eruptions*. *J. Appl. Volcanol.* 2 (1), 1–9.
- Bernard, B., Battaglia, J., Proaño, A., Hidalgo, S., Vásquez, F., Hernandez, S., Ruiz, M., 2016. Relationship between volcanic ash fallouts and seismic tremor: quantitative assessment of the 2015 eruptive period at Cotopaxi volcano, Ecuador. *Bull. Volcanol.* <http://dx.doi.org/10.1007/s00445-016-1077-5>.
- Bobrowski, N., Honninger, G., Galle, B., Platt, U., 2003. Detection of bromine monoxide in a volcanic plume. *Nature* 423 (6937), 273–276.
- Cashman, K.V., Hoblitt, R.P., 2004. Magmatic precursors to the 18 May 1980 eruption of Mount St. Helens, USA. *Geology* 32 (2), 141–144.
- Cioni, R., D’Orlando, C., Bertagnini, A., 2008. Fingerprinting ash deposits of small scale eruptions by their physical and textural features. *J. Volcanol. Geotherm. Res.* 177, 277–287.
- Cioni, R., Pistolesi, M., Bertagnini, A., Bonadonna, C., Hoskuldsson, A., Scateni, B., 2014. Insights into the dynamics and evolution of the 2010 Eyjafjallajökull summit eruption (Iceland) provided by volcanic ash textures. *Earth Planet. Sci. Lett.* 394, 111–123.
- Cordonnier, B., Caricchi, L., Pistone, M., Castro, J., Hess, K.U., Gottschaller, S., Manga, M., Dingwell, D.B., Burlini, L., 2012. The viscous–brittle transition of crystal-bearing silicic melt: direct observation of magma rupture and healing. *Geology* 40, 611–614.
- Dinger, F., Arellano, S., Battaglia, J., Bobrowski, N., Galle, B., Hernandez, S., Hidalgo, S., Hörmann, C., Lübcke, P., Platt, U., Ruiz, M., Warnach, S., Wagner, T., 2016. Variations of the BrO/SO₂ molar ratios during the 2015 Cotopaxi eruption. *European Geosciences Union General Assembly 2016*, Abstract EGU2016-1001.
- Eichelberger, J.C., Carrigan, C.R., Westrich, H.R., Price, R.H., 1986. Nonexplosive silicic volcanism. *Nature* 323 (6089), 598–602.
- Ersoy, O., Chinga, G., Aydar, E., Gourgand, A., Evren Cubukcu, H., Ulusoy, I., 2006. Texture discrimination of volcanic ashes from different fragmentation mechanisms: a case study, Mount Nemrut stratovolcano, eastern Turkey. *Comput. Geosci.* 32 (7), 936–946.
- Eychenne, J., Pennec, J.-L., Troncoso, L., Gouhier, M., Nedelec, J.-M., 2012. Causes and consequences of bimodal grain-size distribution of tephra fall deposited during the August 2006 Tungurahua eruption (Ecuador). *Bull. Volcanol.* 74 (1), 187–205.
- Eychenne, J., Le Pennec, J.-L., Ramón, P., Yepes, H., 2013. Dynamics of explosive paroxysms at open-vent andesitic systems: high-resolution mass distribution analyses of the 2006 Tungurahua fall deposit (Ecuador). *Earth Planet. Sci. Lett.* 361, 343–355.
- Hall, M., Mothes, P., 2008. The rhyolitic–andesitic eruptive history of Cotopaxi volcano, Ecuador. *Bull. Volcanol.* 70 (6), 675–702.
- Hall, M., Ramón, P., Mothes, P., LePennec, J.L., García, A., Samaniego, P., Yepes, H., 2004. Volcanic eruptions with little warning: the case of Volcán Reventador’s Surprise November 3, 2002 Eruption, Ecuador. *Rev. Geol. Chile* 31, 349–358.
- Hammer, E.J., Rutherford, M.J., 2002. An experimental study of the kinetics of decompression-induced crystallization in silicic melt. *J. Geophys. Res. Solid Earth* 107 (B1) (ECV 8-1-ECV 8-24).

- Hammer, E.J., Cashman, V.K., Hoblitt, P.R., Newman, S., 1999. Degassing and microlite crystallization during pre-climactic events of the 1991 eruption of Mt. Pinatubo, Philippines. *Bull. Volcanol.* 60 (5), 355–380.
- Hickey, J., Gottsmann, J., Mothes, P., 2015. Estimating volcanic deformation source parameters with a finite element inversion: the 2001–2002 unrest at Cotopaxi volcano, Ecuador. *J. Geophys. Res. Solid Earth* 120 (3), 1473–1486.
- Hidalgo, S., Bernard, B., Battaglia, J., Gaunt, E., Barrington, C., Andrade, D., Ramón, P., Arellano, S., Yepes, H., Proaño, A., Almeida, S., Sierra, D., Dinger, F., Kelly, P., Parra, R., Vallejo, S., Bobrowsky, N., Galle, B., Almeida, M., Mothes, P., Alvarado, A., Ruiz, M., 2016. IGEPN Cotopaxi volcano's unrest and eruptive activity in 2015: mild awakening after 73 years of quiescence. *Geophys. Res. Abstr.* 18 (EGU2016-5043-1, 2016 EGU General Assembly 2016).
- Houghton, B.F., Wilson, C.J.N., 1989. A vesicularity index for pyroclastic deposits. *Bull. Volcanol.* 51 (6):451–462. <http://dx.doi.org/10.1007/BF01078811>.
- IGEPN Special Report No. 22, November 6, 2015, <http://www.igeppn.edu.ec/cotopaxi//informes-cotopaxi/coto-especiales/coto-e-2015/13703-informe-especial-cotopaxi-n-22/file>.
- Jaupart, C., 1998. Gas loss through conduit walls during eruption. *Geol. Soc. Lond., Spec. Publ.* 145, 73–90.
- Kueppers, U., Scheu, B., Spieler, O., Dingwell, D.B., 2006. Fragmentation efficiency of explosive volcanic eruptions: a study of experimentally generated pyroclasts. *J. Volcanol. Geotherm. Res.* 153, 125–135.
- Kushnir, A.R.L., Martel, C., Bourdier, J.-L., Heap, M.J., Reuschlé, T., Erdmann, S., Komorowski, J.-C., Cholik, N., 2016. Probing permeability and microstructure: unravelling the role of a low-permeability dome on the explosivity of Merapi (Indonesia). *J. Volcanol. Geotherm. Res.* 316, 56–71.
- Macdonald, G.A., 1972. *Volcanoes*. Prentice-Hall, Englewood Cliffs, NJ (510 pp.).
- Mayer, K., Scheu, B., Montanaro, C., Yilmaz, T.I., Isaia, R., Alsbichler, D., Dingwell, D.B., 2016. Hydrothermal alteration of surficial rocks at Solfatara (Campi Flegrei): petrophysical properties and implications for phreatic eruption processes. *J. Volcanol. Geotherm. Res.* 320, 128–143.
- Miwa, T., Toramaru, A., Iguchi, M., 2009. Correlations of volcanic ash texture with explosion earthquakes from vulcanian eruptions at Sakurajima volcano, Japan. *J. Volcanol. Geotherm. Res.* 184 (3–4), 473–486.
- Miwa, T., Geshi, N., Shinohara, H., 2013. Temporal variation in volcanic ash texture during a vulcanian eruption at the Sakurajima volcano, Japan. *J. Volcanol. Geotherm. Res.* 260, 80–89.
- Molina, I., Kumagai, H., García-Aristizábal, A., Nakano, M., Mothes, P., 2008. Source process of very-long-period events accompanying long-period signals at Cotopaxi Volcano, Ecuador. *J. Volcanol. Geotherm. Res.* 176 (1), 119–133.
- Mothes, P.A., Vallance, J.W., 2015. Chapter 6 - lahars at Cotopaxi and Tungurahua volcanoes, Ecuador: highlights from stratigraphy and observational records and related downstream hazards A2 - papale. In: Shroder, J.F., Paolo (Eds.), *Volcanic Hazards, Risks and Disasters*. Elsevier, Boston, pp. 141–168.
- Nakada, S., Motomura, Y., 1999. Petrology of the 1991–1995 eruption at Unzen: effusion pulsation and groundmass crystallization. *J. Volcanol. Geotherm. Res.* 89 (1–4), 173–196.
- Ono, K., Watanabe, K., Hoshizumi, H., S-i, I., 1995. Ash eruption of the Naka-dake crater, Aso volcano, southwestern Japan. *J. Volcanol. Geotherm. Res.* 66 (1–4), 137–148.
- Pardo, N., Cronin, S.J., Nemeth, K., Brenna, M., Schipper, C.I., Breard, E., White, J.D.L., Procter, J., Stewart, B., Agustin-Flores, J., Moebis, A., Zernack, A., Kereszturi, G., Lube, G., Auer, A., Neall, V., Wallace, C., 2014. Perils in distinguishing phreatic from phreatomagmatic ash; insights into the eruption mechanisms of the 6 August 2012 Mt. Tongariro eruption, New Zealand. *J. Volcanol. Geotherm. Res.* 286, 397–414.
- Pistolesi, M., Rosi, M., Cioni, R., Cashman, K.V., Rossotti, A., Aguilera, E., 2011. Physical volcanology of the post-twelfth-century activity at Cotopaxi volcano, Ecuador: behavior of an andesitic central volcano. *Geol. Soc. Am. Bull.* 123, 1193–1215.
- Pistone, M., Arzilli, F., Dobson, K.J., Cordonnier, B., Reusser, E., Ulmer, P., Marone, F., Whittington, A.G., Mancini, L., Fife, J.L., Blundy, J.D., 2015. Gas-driven filter pressing in magmas: insights into in-situ melt segregation from crystal mushes. *Geology* 43, 699–702.
- Ruiz, M., Bertrand, G., Chatelain, J.-L., Yepes, H., Hall, M., Ramon, P., 1998. Possible causes for the seismic activity observed in Cotopaxi Volcano, Ecuador. *Geophys. Res. Lett.* 25 (13), 2305–2308.
- Samaniego, P., Eissen, J.-P., Le Pennec, J.-L., Robin, C., Hall, M.L., Mothes, P., Chavrit, D., Cotten, J., 2008. Pre-eruptive physical conditions of El Reventador volcano (Ecuador) inferred from the petrology of the 2002 and 2004–05 eruptions. *J. Volcanol. Geotherm. Res.* 176 (1), 82–93.
- Savov, I.P., Luhr, J.F., Navarro-Ochoa, C., 2008. Petrology and geochemistry of lava and ash erupted from Volcán Colima, Mexico, during 1998–2005. *J. Volcanol. Geotherm. Res.* 174 (4), 241–256.
- Scandone, R., Cashman, K.V., Malone, S.D., 2007. Magma supply, magma ascent and the style of volcanic eruptions. *Earth Planet. Sci. Lett.* 253 (3–4), 513–529.
- Shea, T., Hammer, J.E., 2013. Kinetics of cooling- and decompression-induced crystallization in hydrous mafic-intermediate magmas. *J. Volcanol. Geotherm. Res.* 260, 127–145.
- Sheridan, M.F., Wohletz, K.H., 1981. Hydrovolcanic explosions: the systematics of water-pyroclast equilibration. *Science* 212 (4501), 1387–1389.
- Sisson, T.W., Bacon, C.R., 1999. Gas-driven filter pressing in magmas. *Geology* 27 (7), 613–616.
- Sparks, R.S.J., 1997. Causes and consequences of pressurisation in lava dome eruptions. *Earth Planet. Sci. Lett.* 150 (3–4), 177–189.
- Sparks, R.S.J., 2003. Forecasting volcanic eruptions. *Earth Planet. Sci. Lett.* 210 (1–2), 1–15.
- Taddeucci, J., Pompilio, M., Scarlato, P., 2002. Monitoring the explosive activity of the July–August 2001 eruption of Mt. Etna (Italy) by ash characterization. *Geophys. Res. Lett.* 29 (8) (71–71–71–74).
- Taddeucci, J., Pompilio, M., Scarlato, P., 2004. Conduit processes during the July–August 2001 explosive activity of Mt. Etna (Italy): inferences from glass chemistry and crystal size distribution of ash particles. *J. Volcanol. Geotherm. Res.* 137 (1–3), 33–54.
- Watanabe, K., Danhara, T., Watanabe, K., Terai, K., Yamashita, T., 1999. Juvenile volcanic glass erupted before the appearance of the 1991 lava dome, Unzen volcano, Kyushu, Japan. *J. Volcanol. Geotherm. Res.* 89 (1–4), 113–121.
- White, J.D.L., Houghton, B.F., 2006. Primary volcanoclastic rocks. *Geology* 34:677–680. <http://dx.doi.org/10.1130/G22346.1>.
- Woods, A.W., Koyaguchi, T., 1994. Transitions between explosive and effusive eruptions of silicic magmas. *Nature* 370 (6491), 641–644.
- Wright, H.M.N., Cashman, K.V., Mothes, P.A., Hall, M.L., Ruiz, A.G., Le Pennec, J.L., 2012. Estimating rates of decompression from textures of erupted ash particles produced by 1999–2006 eruptions of Tungurahua volcano, Ecuador. *Geology* 40 (7), 619–622.